Photofabrication of Fullerene-Shelled Quantum Dots Supramolecular Nanoparticles for Solar Energy Harvesting

Edakkattuparambil Sidharth Shibu,[†] Akinari Sonoda,[†] Zhuoqiz Tao,[‡] Qi Feng,[‡] Akihiro Furube,[§] Sadahiro Masuo,[⊥] Li Wang,[⊥] Naoto Tamai,[⊥] Mitsuru Ishikawa,[†] and Vasudevanpillai Biju[†,∥,*]

[†]Health Research Institute, National Institute of Advanced Industrial Science and Technology (AIST), Takamatsu, Kagawa 761-0395, Japan, [‡]Department of Advanced Materials Science, Kagawa University, Takamatsu, Kagawa 761-0396, Japan, [§]Research Institute for Instrumentation Frontier, AIST, Tsukuba, Ibaraki 305-8565, Japan, [⊥]Department of Chemistry, Kwansei Gakuin University, 2-1 Gakuen, Sanda 669-1337, Japan, and [∥]PRESTO, Japan Science and Technology Agency, Tokyo 332-0012, Japan

ABSTRACT Quantum dots-based electron donor-acceptor systems play a rising role in the design of renewable and carbon-free energy harvesting technologies. In this article, we discuss the photofabrication of fullerene-shelled quantum dots supramolecular nanoparticles, in which the fullerene shell acts as not only a well-defined electron acceptor but also a robust protecting layer against the photocorrosion of the quantum dot core. We evaluate the ensemble and single-molecule electron transfer from the core to the shell in the nanoparticles and the photocurrent response of a photoelectrochemical cell constructed using the nanoparticles. The supramolecular nanoparticle has been prepared by the covalent tethering of a fullerene-thiol monolayer to the quantum dot followed by the photochemical reactions of free fullerene-thiol to the tethered monolayer. The nanoparticles are characterized using scanning electron microscopy, atomic force microscopy, and X-ray photoelectron spectroscopy. Correlated single-photon emission and the two-state ON-OFF photoluminescence show that single quantum dots are included in the supramolecular nanoparticles. The fullerene-shells suppress the blinking of single quantum dots by acting as well-defined electron traps, without allowing the transfer of Auger electrons to unknown traps. Electron transfer from the quantum dot-core to the fullerene-shell is apparent from the short ON and OFF durations in the photoluminescence intensity trajectories of single quantum dots, quenching of the photoluminescence intensity and lifetime of quantum dots at the ensemble level, and the characteristic transient absorption band of the anion radical of fullerene. We next construct a photoelectrochemical cell using the supramolecular nanoparticles, and the transferred electron is externally driven in the cell to generate ~400 μA/cm^2 photocurrent. Electron transfer from the highly stable quantum dots to the protecting fullerene-shells places the supramolecular nanoparticles among the most promising antenna systems for the construction of cost-effective and stable next generation solar energy harvesting systems.

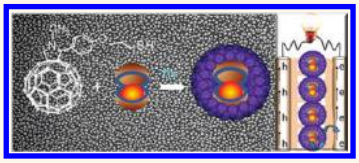

KEYWORDS: supramolecular nanoparticles · quantum dots · C_{60} · electron transfer · single-molecule · solar cell · donor-acceptor system

Renewable resources of carbon-free energy is crucial in the current scenario of global warming and our growing energy needs.[1] Besides, the significance of safer energy resources has been underscored by many recent nuclear mishaps, including the recently crippled Fukushima Nuclear Power Plant in Japan.[2] Sunlight is the most promising alternative to nuclear fuels and greenhouse gas emitting fossil and alcohol fuels. Although solar energy can efficiently be converted into thermal energy, generation of electrical energy at high efficiency using photovoltaic devices is essential to drive our equipments. To-date, the most widely investigated solar cells are designed from polycrystalline silicon[3] or dye sensitized mesoporous TiO_2.[4] Although photocurrent efficiency of commercial solar cells is as low as 15%, recent advances in the solar energy research have provided us with hopeful experimental efficiencies exceeding 28%.[5,6] The narrow absorption bands of photosensitizers and energy-wasting back electron transfer are two major limitations in the advancement of solar cell technology. These limitations underline the importance of developing novel electron donor-acceptor antenna systems for both cosseting our demand for safe but carbon-free energy and offsetting the greenhouse effects.

Semiconductor quantum dots (QDs) have become promising electron donors in the construction of the next generation solar cells.[7−22] The QD-based electron donor−acceptor systems are analogous to the conventional organic donor-acceptor systems based on porphyrins,[23−28] oligothiophenes,[29,30] fulvalenes,[31,32] carotenyls,[33] and amines.[34−36] The most investigated QD-based donor-acceptor systems are QD-TiO_2,[12,14,15] QD-C_{60},[16−20] and QD-tin oxide.[21,22] In these systems, QDs are promising light absorbers and electron donors owing to their broad absorption in the solar spectrum, large molar extinction coefficient, and exceptional photostability.[37−42] Furthermore, the ability of QDs to activate multiple exciton pairs at the cost of a single photon will be advantageous for the construction of high-efficiency solar cells.[43] Similarly, C_{60} is a promising electron acceptor owing to its broadband absorption in the

* Address correspondence to v.biju@aist.go.jp.

Received for review November 23, 2011 and accepted January 19, 2012.

Published online January 19, 2012
10.1021/nn204567d

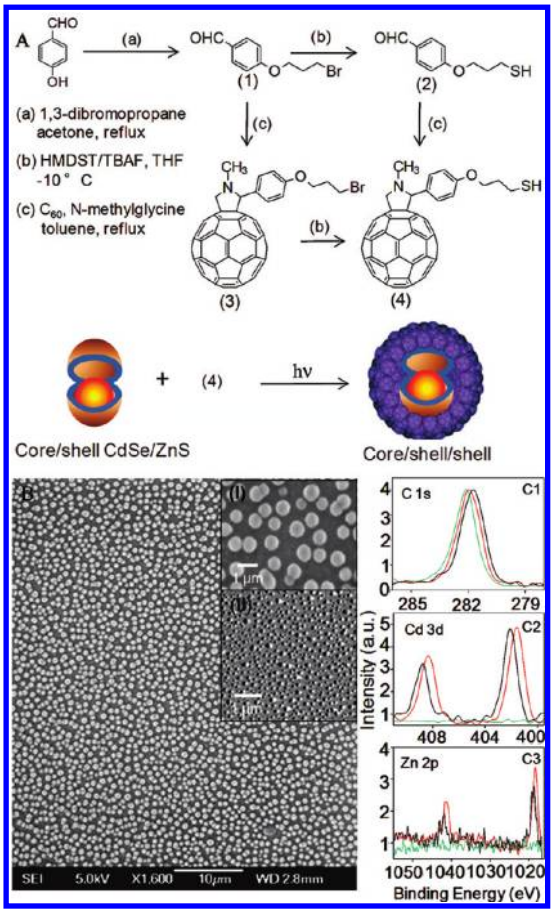

Figure 1. (A) Scheme for the synthesis of a C_{60} thiol derivative and SNPs. (B) FESEM image of SNPs. Inset: (i) high-magnification FESEM image and (ii) tapping mode AFM image of SNPs. (C) X-ray photoelectron spectra (XPS) of (C1) C 1s, (C2) Cd 3d, and (C3) Zn 2p regions for C_{60} (green), QD (red), and SNPs (black), respectively.

visible to NIR region, photostability, and ability to accommodate multiple electrons.[44] Nevertheless, supramolecular donor-acceptor nanoparticles composed of C_{60} and QDs are yet to be exploited in detail. Although the potentials of C_{60}/TiO_2/ITO as electron acceptor and QD as electron donor were extensively investigated, practical applications of QDs in I^-/I_3^- coupled solar cells is limited by the photocorrosion of QDs caused by iodine.[45]

This article is a report on the preparation of fullerene-shelled QDs supramolecular nanoparticles (SNPs), a model donor-acceptor antenna system for solar energy harvesting. Additionally, the fullerene shell acts as a protecting layer of QDs against its photocorrosion in the I^-/I_3^- couple. Here, we investigated the effect of C_{60} shells on both Auger ionization of QDs and the fate of the Auger ionized QDs by recording and analyzing the photoluminescence (PL) intensity trajectories, the PL decay profiles, and the transient absorption (TA) spectra of SNPs at ensemble and single-molecule levels. Interestingly, long-living ON and OFF states in the single-molecule PL intensity trajectories were absent after the caging of QDs in the C_{60} shells. Also, photoinduced electron transfer from QD to C_{60} results in the generation of a C_{60} anion radical, which was detected using TA spectroscopy. On the basis of these observations, we hypothesize that C_{60} shells act as well-defined electron traps for QDs, without allowing Auger electron transfer from the QD core to an unknown trap. Also, the reduced OFF time in the PL intensity trajectories of the SNP suggests that the C_{60} shell accommodates the transferred electron, which subsequently recombines with an excess positive charge in the core. Thus, the C_{60} shell lowers the possibility of energy-wasting nonradiative relaxations in Auger ionized QD, which otherwise relaxes nonradiatively until neutralized. We next constructed a photoelectrochemical cell using the SNPs, and the transferred electron was externally driven in the cell to generate stable photocurrent up to 400 $\mu A/cm^2$. Thus, the fullerene-shell acts as not only a well-defined electron acceptor but also a physical protection layer against the photocorrosion of QDs.

RESULTS AND DISCUSSION

Figure 1A shows steps involved in the preparation of a C_{60}-thiol derivative and C_{60} shells on QDs. The SNPs were prepared by the tethering of a C_{60}-thiol monolayer to the ZnS shells on CdSe QDs followed by UV (256 nm) induced [2 + 2] cycloaddition reactions[46] of excess C_{60}-thiol with the tethered C_{60} monolayer. The [2 + 2] cycloaddition reaction among C_{60} moieties was confirmed on the basis of characteristic vibrational bands (Supporting Information) in the FT-IR spectrum (Figure S1). Detailed procedure of the synthesis of the C_{60}-thiol derivative and characterization of the intermediates in Figure 1A are provided in the Experimental Section. The morphology of the SNPs was analyzed using field emission scanning electron microscopy (FESEM) and atomic force microscopy (AFM). A large area FESEM image of the SNPs is shown in Figure 1B. Interestingly, the size (300 ± 50 nm) and shape (spheroid) of the SNPs are uniformly distributed. A zoomed-in and scanned FESEM image of the SNPs is shown in the inset (i) of Figure 1B. Distribution of the size and shape of the SNPs was further characterized by recording and analyzing tapping mode AFM images. A typical AFM image of the SNPs is shown in the inset (ii) of Figure 1B. The formation of thick C_{60} shells on QDs can be attributed to [2 + 2] cycloaddition reactions[46] of free C_{60} molecules present in the solution with the tethered C_{60} molecules. In contrast, we did not find any SNPs formed in a mixture of QDs and pristine C_{60} after photoactivation. Thus, we hypothesize that the tethered C_{60}-thiol monolayer acts as a nucleation layer for the photoreaction and the formation of the core-shell SNPs. The QD-C_{60} core-shell nanoparticle was further characterized using X-ray photoelectron spectroscopy (XPS). The characteristic bands of C 1s, Cd 3d, and Zn 2p in C_{60}, QDs, and SNPs are shown in Figure 1C.

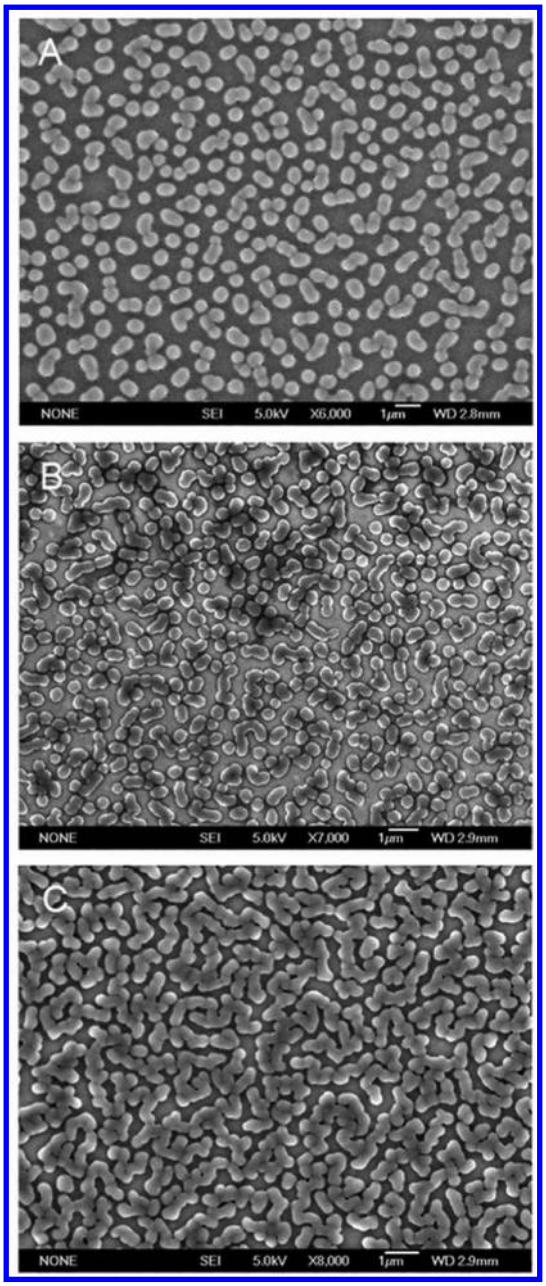

Figure 2. FESEM images of SNPs obtained after photoactivation of C_{60}-thiol layered CdSe/ZnS QDs for different time intervals: (A) 2 h, (B) 4 h, and (C) 6 h.

The binding energy values of C 1s, Cd 3d, and Zn 2p are comparable to those reported previously.[47] The major bands of C, Cd, and Zn in XPS support the structure perceived for SNP from FT-IR, FESEM, and AFM data.

To further evaluate the cycloaddition reaction, we have studied the temporal effects on the photoactivation of C_{60}-thiol layered CdSe/ZnS QDs by mapping the SEM images at different time intervals (2, 4, and 6 h). With time under photoactivation, the spherical SNPs were gradually elongated and then transformed into linear and branched nanoparticles as shown in Figure 2A–C. We hypothesize that the temporal evolution of the linear and branched structures occurs as a result of either photocycloaddition among the spherical SNPs or the photochemical reactions of free C_{60}-thiol with the spherical SNPs. However, we found that the linear and branched structures can be formed even without the addition of excess C_{60}-thiol to the spherical SNPs, which rules out the possibility that the linear structures can be formed by the gradual photocycloaddition of free C_{60}-thiol with the spherical SNPs. On the other hand, the linear and branched nanoparticles are not formed without photoactivation of the spherical SNPs. Thus, we assume that the linear and branched nanoparticles are formed by the photocycloaddition among spherical SNPs. Furthermore, the morphologies of the nanoparticles (Figure 2C) suggest that the linear and branched structures are most probably formed by the photochemical fusion among the spherical SNPs.

We next evaluated the effect of C_{60} shells on the PL properties of QDs by recording and analyzing the PL intensity trajectories of single QDs and single SNPs. Single-molecule samples were prepared by spin-coating of 10 pM solutions of QD or the SNP on coverslips. Panels A and B in Figure 3 show typical PL intensity trajectories of a pristine QD and a SNP. Also, statistical distributions of ON and OFF times of 100 QDs and 100 SNPs are shown in panels C–F in Figure 3. The two-state ON-OFF PL intensity trajectories (Figure 3A,B) detected for ~80% fluorescent spots in the single-molecule samples suggest that single QDs are incorporated in the SNPs. Furthermore, photon correlation measurements on single SNPs were carried out using a combined Hanbury–Brown–Twiss photon coincidence system, and a sample-scanning confocal fluorescence microscope show single photon emission from individual SNPs (Figure 3G). Thus, we assume that single QDs are included in individual SNPs. On the other hand, we should expect uncorrelated photons for SNPs encapsulated with multiple QDs. Interestingly, as C_{60} shells were prepared on QDs, the number of ON events in the PL intensity trajectories (panel B) is increased with a concomitant decrease of both ON and OFF times. Precisely, OFF time exceeding 50 s (panel D in Figure 3) and ON time exceeding 5 s (panel F in Figure 3) were rare in the histograms of SNPs. On the other hand, several OFF events with durations in the 50–200 s scale and ON events with durations in the 5–50 s scale were detected for pristine QD. In general, blinking of single QDs can be explained by a simple "charge trapping model"[48] in which a photoexcited QD ejects out an electron and creates excess positive charge in the core. In PL intensity trajectories, ON time corresponds to the average time during which a QD stays in the neutral state. Thus, a decrease in the occurrences of long-living ON events for the SNPs, although minor, should be suggestive of an increase in the rate of charge carrier trapping in the defect state, which is a C_{60} shell in the SNP. In other words, the short ON time suggests that electron transfer from

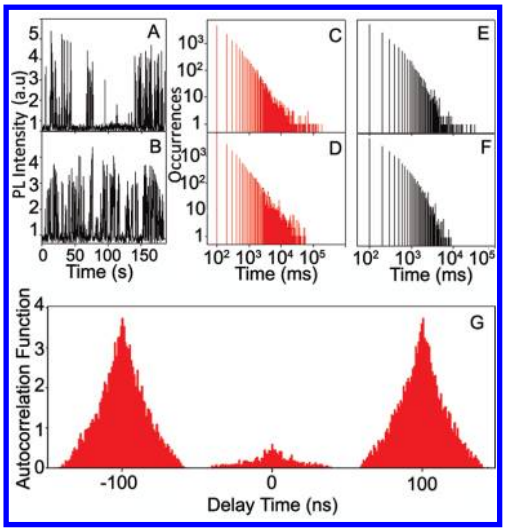

Figure 3. (A, B) PL intensity trajectories of a pristine QD (A) and a SNP (B). (C,D) OFF time distributions for single QDs (C) and SNPs (D). (E,F) ON time distributions for 100 single QDs (E) and 100 single SNPs (F). (G) Photocount histogram of arrival time under pulsed excitation, showing the antibunching behavior of single SNPs.

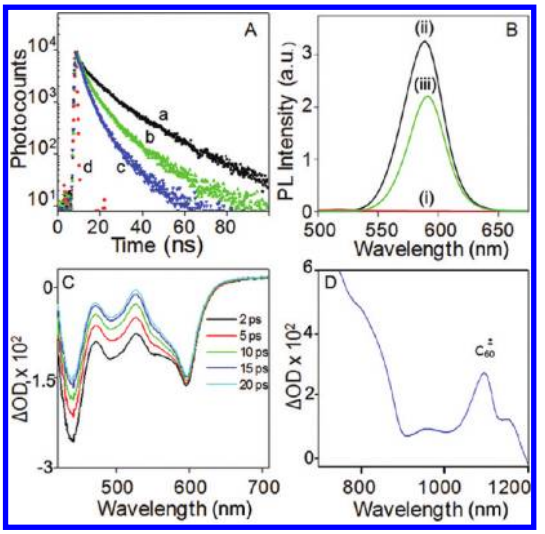

Figure 4. (A) PL decay profiles of pristine QDs (a), a mixture of QDs and C_{60} (b), SNPs (c), and the instrument response function (d). (B) PL spectra (λ_{ex} = 450 nm) of C_{60}-thiol (i), QD (ii), and SNPs (iii). (C) Femtosecond TA spectra of SNPs recorded at different time intervals. (D) Nanosecond TA spectrum of SNPs showing the anion radical of C_{60}.

photoactivated QD to a C_{60} shell is operative in the SNPs. On the other hand, OFF time represents duration of a QD in the Auger ionized state, and the long-living OFF states represent an ionized QD waiting to be neutralized. Thus, a decrease in the occurrences of long-living OFF events for the SNPs, although minor, should be suggestive of an increase in the rate of charge recombination or neutralization of Auger ionized QD. Indeed, QDs with long-living OFF states are less promising systems for solar energy harvesting because, although an ionized QD continuously absorbs light, the energy wasting nonradiative relaxation will be dominant due to energy transfer between a subsequently activated exciton and excess positive charge in the trion. Thus, short ON and OFF times suggest that QDs caged in C_{60} shells can be ideal antenna systems for solar cells.

The role of the C_{60} shell on trapping of an electron from a photoactivated QD was further investigated by recording and analyzing the PL decay profiles of pristine QDs, a mixture of QDs and C_{60}, and the SNPs. Samples for PL decay measurements were prepared by spin-coating of 10 pM solutions on coverslips. Traces a, b, and c in Figure 4A show the PL decay profiles of pristine QDs, a mixture of QDs and C_{60}, and the SNPs, respectively. These decay profiles indicate efficient quenching of the excited state of QDs by C_{60}. The PL decay curves were fitted using a third order function. Corresponding PL spectra of QDs, the SNPs, and C_{60}-thiol are shown in Figure 4B. The PL lifetime of the SNP was short (τ_{av} = 1.87 ns) compared to that of pristine QD (τ_{av} = 4.68 ns), indicating the deactivation of the core QD by electron transfer to the C_{60} shell. Also, the PL lifetime (τ_{av} = 2.23 ns) of QD in the mixed samples was intermediate between that of pristine QD and the SNP. The average lifetime values are estimated as $\tau_{av} = (\tau_1\alpha_1 + \tau_2\alpha_2 + \tau_3\alpha_3)/(\alpha_1 + \alpha_2 + \alpha_3)$, where τ_1, τ_2, and τ_3 are the individual lifetime values and α_1, α_2, and α_3 are the corresponding amplitues. On the basis of these lifetime values, the average rate of electron transfer in the SNPs is estimated at $3.2 \times 10^8\ s^{-1}$, which is intermediate between the rates detected for electron transfer from QDs to ITO[22] and TiO_2 NPs.[15] On the other hand, the rate of electron transfer for QD-C_{60} single-molecules is known to largely fluctuate from dot to dot in the $0.25 \times 10^9\ s^{-1}$ to $\sim 1.5 \times 10^9\ s^{-1}$ scale.[17] The difference in the rates of electron transfer can be assigned to fluctuations in the interfacial coupling between the donor and acceptor moieties.[49] The above lifetime value of SNP is consistent with the short ON time (Figure 3F). In other words, on the basis of the short ON time and PL lifetime (Figure 4A) values, it is apparent that the C_{60} shell traps an electron from the core QD.

To correlate among ON and OFF times, PL lifetime values, electron transfer, and Auger ionization processes, we recorded the TA spectra of QDs and the SNPs and analyzed the kinetics of bleach and recovery. Samples for TA measurements were prepared by dispersing QDs or SNPs in *o*-xylene at 0.1 μM. These samples were excited with 100 fs or 150 ps laser pulses in pump−probe spectrometer systems, and the TA spectra were recorded at different femtosecond, picosecond, and nanosecond time intervals. Figure 4C shows the femtosecond time-resolved bleach-recovery of SNPs. Steady-state absorption spectra, the bleach recovery of QDs and the kinetics of bleach recovery

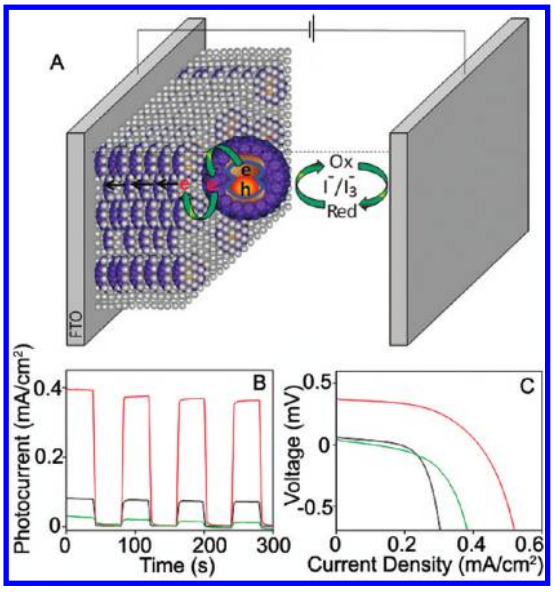

Figure 5. (A) Design of a photoelectrochemical cell sensitized by SNPs. (B) Photocurrent response under ON-OFF cycles of simulated sunlight of AM 1.5 (100 mW/cm^2) and (C) *I*−*V* characteristics of the cells. (B,C) C_{60}-thiol (green), QDs only (black), and SNPs (red).

at 432, 490, 550, and 590 nm for both QDs, and SNP are shown in the Supporting Information (Figures S2 and S3). There were no significant changes in the rates of bleach and recovery in the 200 fs to 1 ns scale. On the other hand, we detected an absorption band ~1070 nm in the nanosecond TA spectra (Figure 4D), which is the characteristic band of the anion radical of C_{60}.[50] Therefore, electron transfer from the QD core to the C_{60} shell is obvious.

To further evaluate the electron transfer process in the SNP, we have constructed three types of photoelectrochemical cells and measured the photocurrent response of the cells. Photosensitizers in the cells were C_{60}-thiol, QD, or SNP. Photoanodes were prepared by the coating of colloidal TiO_2 solution on fluorine-tin-oxide (FTO) plates followed by calcination of the plates at 400 °C for 30 min. Subsequently, C_{60}-thiol, QD, or SNP was absorbed into the anode and dried at room temperature. Photoelectrochemical cells were assembled as shown in Figure 5A by placing I^-/I_3^- electrolyte in between the photoanode and Pt counter electrode. In the photoelectrochemical cell, individual SNPs are probably surrounded by the electrolyte, which permits the hole-collection. The electrolyte was prepared by dissolving butylmethylimidazolium iodide (0.60 mol/L), I_2 (0.03 mol/L), guanidinium thiocyanate (0.10 mol/L), and 4-*tert*-butylpyridine (0.50 mol/L) in a mixture (85%/15% v/v) of acetonitrile and valeronitrile. A photocurrent response of the cells was measured under simulated sunlight of AM 1.5 (100 mW/cm^2). Figure 5B,C shows the photocurrent response and *I*−*V* characteristics under ON-OFF cycles of simulated sunlight for cells constructed using SNP, QD, and C_{60}-thiol. The maximum photocurrent and open circuit voltage generated in SNP-based photoelectrochemical cell were 395 μA/cm^2 and 37 mV. These values are greater than that for C_{60}-thiol or QD-based cells. Constant photocurrent under repeated ON-OFF cycles of illumination (Figure 5B) is indicative of the stability of SNP and the reproducibility of photocurrent. The stable photocurrent response of the SNP-based solar cell further supports efficient photoinduced electron transfer from QD to C_{60} shell. Here the supplementary role of the fullerene shells is to protect the quantum dots against chemical etching in the red-ox couple. It is well-known that iodine in the I^-/I_3^- red-ox couple causes the photocorrosion of QDs,[44] which results in the significant loss of photovoltage in many reported solar cells. The fullerene-shells in the current system protect QDs against such photocorrosion and permit stable operation of the photoelectrochemical cell.

CONCLUSIONS

We have synthesized novel fullerene-shelled quantum dots supramolecular nanoparticles by the covalent tethering of a fullerene-thiol monolayer to the quantum dot followed by the photochemical reactions of free fullerene-thiol to the tethered monolayer. The SNPs were characterized using FESEM, AFM, and X-ray photoelectron spectroscopy. Inclusion of single quantum dots in individual nanoparticles is apparent from the correlated single-photon emission behavior and the two-state ON-OFF photoluminescence characteristics of the SNPs. The fullerene-shells considerably suppress the blinking of single quantum dots by acting as electron traps, without allowing the transfer of Auger electrons to unknown traps. Electron transfer from the quantum dot-core to the fullerene-shell is apparent from the short ON and OFF durations in the photoluminescence intensity trajectories of single quantum dots, quenching of the photoluminescence intensity and lifetime of quantum dots, and the characteristic transient absorption band of the anion radical of fullerene. These results suggest that the fullerene-shells in the nanoparticles act as well-defined electron traps. The trapped electron subsequently recombines with the excess positive charge in the core quantum dot, and thus the shells not only lower the lifespan of Auger ionized quantum dots but also suppress the energy-wasting nonradiative relaxations in Auger ionized quantum dots. We next constructed a photoelectrochemical cell using the supramolecular nanoparticles, and the transferred electron was externally driven in the cell. Here the supplementary role of the fullerene shells in the supramolecular nanoparticles is to protect the quantum dots against chemical etching or photocorrosion by iodine in the I^-/I_3^- red-ox couple and permit stable operation of the solar cell. Electron transfer from the

highly stable quantum dot to the protecting fullerene-shell places the supramolecular nanoparticles among the most promising antenna systems for solar energy harvesting.

EXPERIMENTAL SECTION

Synthesis of Compound 1. A suspension of 1,2-dibromopropane (4 g, 20 mmol), *p*-hydroxybenzaldehyde (1.22 g, 10 mmol), and K_2CO_3 (2.76 g, 20 mmol) was refluxed in acetone (25 mL) for 12 h. The reaction mixture was cooled, filtered, and concentrated under reduced pressure. The crude product was chromatographed over silica gel (200−400 mesh) and eluted with chloroform to give 85% of compound **1**. ^{1}H NMR (400 MHz, $CDCl_3$) δ 9.9 (s, 1H), 7.8−7.9 (m, 2H), 6.95−7.1 (m, 2H), 4.15−4.25 (t, 2H), 3.45−3.55 (t, 2H), 2.15−2.35 (m, 2H). ^{13}C NMR (125 MHz, $CDCl_3$) δ 190.89, 163.89, 132.18, 130.38, 118.48, 114.99, 69.20, 65.91, 32.27, 29.78. FT-IR (ν_{max}), 3362, 3068, 2946, 2738, 1682, 1602, 1505, 1309, 1248, 1157, 1022, 826, 661 cm^{-1}.

Synthesis of Compound 2. A stirred solution of compound **1** (0.61 g, 3.2 mmol) in THF (2 mL) was cooled to −10 °C followed by adding a mixture of hexamethyldisilathiane (HMDST, 1.2 equiv) and tetrabutylammonium bromide (TBAF, 1.1 equiv) dissolved in THF (1 mL). The mixture was warmed to room temperature while being stirred. After 12 h, the reaction mixture was diluted with dichloromethane and washed with saturated NH_4Cl solution. The crude product when chromatographed over silica gel (200−400 mesh) and eluted with 20% ethyl acetate/hexane mixture gave 65% of compound **2**. ^{1}H NMR (400 mHz, $CDCl_3$), δ 9.9 (s, 1H), 7.81−7.86 (m, 3H), 6.9−7.0 (d, 1H), 4.16−4.20 (t, 2H), 2.7−2.8 (dt, 2H), 2−2.2 (m, 2H), 1.38−1.44 (t, 1H). ^{13}C NMR (125 MHz, $CDCl_3$), δ 190.92, 164.08, 132.19, 130.28, 114.97, 66.22, 33.25, 21.27. FT-IR (ν_{max}), 3362, 3190, 2922, 2872, 2745, 2573, 2017, 1907, 1706, 1590, 1303, 1236, 1162, 1046, 845 cm^{-1}.

Synthesis of Compound 3. A mixture of C_{60} (720 mg, 1 mmol), compound **1** (242 mg, 1 mmol), and *N*-methylglycine (267 mg, 3 mmol) in toluene (145 mL) was stirred under reflux for 12 h. The reaction mixture was cooled, and removal of the solvent under reduced pressure gave a solid residue. The residue when chromatographed over silica gel (200−400 mesh) and eluted with toluene gave 45% of compound **2**. ^{1}H NMR (400 MHz, $CDCl_3$), δ 7.7 (br.s, 2H), 6.93−7.02 (d, 2H), 5 (d, 1H), 4.89 (s, 1H), 4.25 (d, 1H), 4.08−4.16 (t, 2H), 3.58−3.66 (t, 2H), 2.80 (s, 3H), 2.28−2.36 (m, 2H). ^{13}C NMR (125 MHz, $CDCl_3$) δ 158.97, 156.61, 154.35, 153.87, 147.53, 147.01, 146.73, 146.36, 146.15, 146.00, 145.46, 144.83, 144.61, 143.32, 143.21, 142.78, 142.51, 142.31, 141.90, 141.76, 140.35, 140.12, 139.80, 137.02, 136.76, 135.96, 130.75, 129.50, 129.23, 128.42, 125.49, 117.93, 114.83, 83.41, 77.51, 77.20, 76.87, 76.55, 70.25, 69.22, 69.02, 65.56, 40.17, 32.67, 31.07, 30.15, 29.89. FT-IR (ν_{max}), 3093, 3031, 2934, 2834, 2867, 2372, 2329, 1596, 1492, 1449, 1376, 1071, 1028, 729, 686, 667, 550 cm^{-1}. LDI-TOF, m/z = 989.

Synthesis of Compound 4 from 2. A mixture of C_{60} (720 mg, 1 mmol), compound **2** (196 mg, 1 mmol), and *N*-methylglycine (267 mg, 3 mmol) in toluene (145 mL) was stirred under reflux for 12 h. The reaction mixture was cooled, and removal of the solvent under reduced pressure gave a solid residue. The residue when chromatographed over silica gel (200−400 mesh) and eluted with toluene gave 65% of compound **4**. Details about characterization of compound **4** are given below.

Synthesis of Compound 4 from 3[46]**.** To a stirred solution of compound **3** (0.6 g, 0.6 mmol) in freshly distilled THF (2 mL), a mixture of HMDST (1.2 equiv) and TBAF (1.1 equiv) dissolved in THF (1 mL) was added. The resulting mixture was stirred at room temperature for 12 h, diluted with dichloromethane, and washed with saturated NH_4Cl solution. The crude product when chromatographed over silica gel (200−400 mesh) and eluted with toluene gave 65% of compound **2**. ^{1}H NMR (400 MHz, $CDCl_3$), δ 7.9 (s, 2H), 6.91−6.95 (d, 2H), 4.91−5.0 (d, 1H), 4.86 (s, 1H), 4.21−4.25 (d, 1H), 4.04−4.09 (t, 2H), 2.79 (s, 3H) 2.68−2.79 (m, 2H), 2.0−2.1 (m, 2H), 1.3−1.4 (t, 2H). ^{13}C NMR (125 MHz, $CDCl_3$) δ 159.12, 156.62, 154.35, 153.89, 153.89, 147.53, 147.02, 146.73, 146.53, 146.38, 146.16, 146.00, 145.76, 145.45, 144.92, 144.61, 144.37, 143.21, 142.90, 142.77, 142.48, 142.32, 142.22, 142.05, 141.90, 141.76, 140.35, 140.12, 139.79, 137.01, 136.76, 135.96, 130.72, 129.34, 114.79, 83.42, 77.51, 77.40, 77.19, 76.87, 76.56, 70.24, 69.22, 65.88, 40.15, 33.61, 21.47. FT-IR (ν_{max}), 3085, 3028, 2940, 2838, 2741, 2500, 1609, 1512, 1467, 1438, 1329, 1290, 1245, 1171, 1097, 1028, 803 cm^{-1}. LDI-TOF, m/z = 944.

^{1}H and ^{13}C NMR spectra of the above four compounds are shown in the Supporting Information (Figure S4).

Preparation of SNPs. SNP was prepared by the mixing of a 10 μM C_{60}-thiol solution in *o*-xylene and a 100 nM solution of CdSe/ZnS QDs in *o*-xylene. During this mixing, a monolayer of C_{60} was formed on the surface of QDs as a result of tethering of thiol to the ZnS shell. Details about conjugation of thiols to ZnS shell can be found elsewhere.[51] Subsequently, the mixture of QD and C_{60}-thiol derivative was photoactivated in a UV trans-illuminator (256 nm) for 2−8 h. This photoreaction provided us with uniform-size and -shape SNPs composed of a C_{60} shell and QD core. The formation of the SNPs is attributed to UV induced [2 + 2] cycloaddition reactions of excess C_{60} thiol with the tethered C_{60} monolayer. UV irradiation for ∼2 h is optimum for the formation of uniform-size spheroid nanoparticles.

Materials and Methods. All the chemicals and solvents were analytical grade and used without further purification. CdSe/ZnS QDs (PL maximum ∼585 nm) was obtained from Invitrogen Corporation. *N*-Methyl glycine, *p*-hydroxy benzaldehyde, HMDST, TBAF, and C_{60} were obtained from Sigma Aldrich, and K_2CO_3, NaOH, and 1,3-dibromopropane were obtained from Wako Chemicals.

Single-molecule experiments were carried out in a far-field video microscopy system composed of an inverted optical microscope (Olympus IX71) that was equipped with a 60× objective lens (Olympus, NA 0.98). Fluorescence signal was filtered through a band-pass filter for QD, magnified using a 3.3× telescopic lens, and recorded using an image intensifier-charge-coupled device (CCD) assembly (Hamamatsu Photonics).

Fluorescence decay profiles were recorded using an assembly of a polychromator and a streak-scope (Hamamatsu Photonics). The excitation light used was 400 nm fs laser pulses from an optical parametric amplifier (OPA). The OPA was pumped by 800 nm pulses (200 kHz) from a regenerative amplifier that was seeded by a mode-locked Ti:Sapphire laser (76 MHz).

Femtosecond TA spectra were measured using a femtosecond pump−probe apparatus. Samples were excited at 400 nm by the second harmonic of an amplified mode-locked Ti:Sapphire laser (Spitfire and Tsunami, Spectra-Physics). Excitation intensity was 0.3 mW at 0.5 kHz. TA spectra were probed using the delayed pulses of a white-light continuum generated by the focusing of fundamental laser pulse (800 nm) into a D_2O cell and detected using an assembly of a polychromator and a CCD (Spectra Pro-275 and Spec-10, Acton Research Co. and Princeton Instruments). The spectral range was 420−780 nm, and the temporal resolution of our detection was 100 fs. The excitation light source for nanosecond TA measurements was the third harmonic (532 nm) of a Nd^{3+}:YAG laser after pulse compression (10 Hz, 150 ps, Ekspla:SL311). A Xe flash lamp (Hamamatsu, L4642) was used as a probe light source. The near-infrared probe light was detected using a fast InGaAs photodetector (New Focus, 1611).

Photon correlation measurements were performed using a Hanbury-Brown-Twiss type photon correlation setup in combination with a home-built sample-scanning confocal fluorescence microscope (IX71, Olympus). The excitation light source used was circularly polarized 405 nm pulses from a pulsed diode laser [10 MHz, 100 ps full width at half-maximum (fwhm), LDH-P-C-405B, picoquant]. The emitted photons from the SNPs were collected using an objective lens (100×; N.A, 1.45; Olympus) and were passed through a 100 μm optical pinhole and a band-pass filter that is suitable for the PL band of the SNPs. Next, the collected PL was divided by a 50/50 nonpolarizing beam splitter into two beam paths and then detected using two avalanche single-photon counting modules (APD, SPCM-AQR-14,

PerkinElmer). The signals from the APDs were connected to a router of a time-correlated single-photon counting (TCSPC) system (SPC630, Becker & Hickl). The signal from one of the two APDs was delayed using a delay generator (DG535, Stanford Research) to compensate for the dead time of the TCSPC board. Time-resolved data were acquired using first-in-first-out mode in which the arrival time, the time delay, and the detection channel were registered for every detected photon. The data were analyzed using a homemade LabVIEW routine that allowed us to evaluate the time traces of fluorescence intensity and the photon correlation histogram of single SNPs.

^{1}H and ^{13}C NMR measurements were carried out in a JEOL 400 MHz spectrometer. LDI-TOF measurements were carried out using a Bruker Microflex. FESEM images were acquired using a JSM-6700FZ (JEOL) microscope operating at 10 μA and 15 kV. Topography images of SNPs were obtained using a MFP-3D AFM (Asylum Research). Tapping-mode AFM images were collected in air, using ultrasharp (radius of curvature <10 nm) silicon cantilevers (Olympus). The cantilevers were ~160 μm long and had a spring constant of ~42 N/m and a resonance frequency of ~300 kHz. XPS measurements was carried out using Kratos (Shimadzu), under a basic pressure of 1.7×10^{-8} Torr, and the X-ray source used was anode mono-Al with pass energy of 40 eV (survey scan). The photocurrent–voltage characteristics of photoelectrochemical cells were measured using a Hokuto-Denko BAS100B electrochemical analyzer under irradiation with simulated sunlight of AM 1.5 (100 mW/cm^2), using a sunlight simulator (YSS-E40, Yamashita Denso) and a 0.25 cm^2 mask.

Conflict of Interest: The authors declare no competing financial interest.

Acknowledgment. We thank D. S. Kumar and R. Sreejith (Toyo University, Japan) for XPS measurements, Y. Shigeri and A. Yasuda (AIST Kansai Centre, Japan) for LDI-TOF mass analyses, and R. Katoh (Nihon University, Japan) for the development of our nanosecond transient absorption system. This work is supported by the Japan Science and Technology Agency (JST) under the Precursory Research for Embryonic Science and Technology (PRESTO) program (to V.B.). Also, E.S.S. acknowledges a postdoctoral fellowship of the Japan Society for the Promotion of Science (JSPS).

Supporting Information Available: Figure S1, FT-IR spectra of SNPs and C_{60}-thiol; Figure S2, UV–vis absorption spectra of C_{60}-thiol, QDs, and SNPs; Figure S3, bleach recovery of QDs and the kinetics of bleach recovery of SNP and QDs; Figure S4, ^{1}H and ^{13}C NMR spectra of C_{60} derivatives. This material is available free of charge *via* the Internet at http://pubs.acs.org.

REFERENCES AND NOTES

1. Kamat, P. V. Meeting the Clean Energy Demand: Nanostructure Architectures for Solar Energy Conversion. *J. Phys. Chem. C* **2007**, *111*, 2834–2860.
2. Global Confidence in Nuclear Energy Falls After Japan Quake, *The Japan Times*, April 19, **2011**.
3. Beaucarne, G.; Slaoui, A. In *Thin Film Solar Cells: Fabrication, Characterization and Applications*; Poortmans, J., Arkhipov, V., Eds.; John Wiley & Sons, Ltd.: Chichester, U.K., 2006; DOI: 10.1002/0470091282.ch3)
4. Bach, U.; Lupo, D.; Comte, P.; Moser, J. E.; Weissortel, F.; Salbeck, J.; Spreitzer, H.; Grätzel, M. Solid-state Dye-Sensitized Mesoporous TiO_2 Solar Cells with High Photon-to-Electron Conversion Efficiencies. *Nature* **1998**, *395*, 583–585.
5. Colodrero, S.; Mihi, A.; Haggman, L.; Ocana, M.; Boschloo, G.; Hagfeldt, A.; Miguez, H. Porous One-Dimensional Photonic Crystals Improve the Power-Conversion Efficiency of Dye-Sensitized Solar Cells. *Adv. Mater.* **2009**, *21*, 764–770.
6. Gratzel, M. Recent Advances in Sensitized Mesoscopic Solar Cells. *Acc. Chem. Res.* **2009**, *42*, 1788–1798.
7. Bang, J. H.; Kamat, P. V. Quantum Dot Sensitized Solar Cells. A Tale of Two Semiconductor Nanocrystals: CdSe and CdTe. *ACS Nano* **2009**, *3*, 1467–1476.
8. Robel, I.; Subramanian, V.; Kuno, M.; Kamat, P. V. Quantum Dot Solar Cells. Harvesting Light Energy with CdSe Nanocrystals Molecularly Linked to Mesoscopic TiO_2 Films. *J. Am. Chem. Soc.* **2006**, *128*, 2385–2393.
9. Kongkanand, A.; Tvrdy, K.; Takechi, K.; Kuno, M.; Kamat, P. V. Quantum Dot Solar Cells. Tuning Photoresponse through Size and Shape Control of CdSe–TiO_2 Architecture. *J. Am. Chem. Soc.* **2008**, *130*, 4007–4015.
10. Pattantyus-Abraham, A. G.; Kramer, I. J.; Barkhouse, A. R.; Wang, X.; Konstantatos, G.; Debnath, R.; Levina, L.; Raabe, I.; Nazeeruddin, M. K.; Grätzel, M.; et al. Depleted-Heterojunction Colloidal Quantum Dots Solar Cells. *ACS Nano* **2010**, *4*, 3374–3380.
11. Yu, X.-Y.; Liao, J.-Y.; Kuang, D.-B.; Su, C.-Y. Dynamic Study of Highly Efficient CdS/CdSe Quantum Dot-Sensitized Solar Cells Fabricated by Electrodeposition. *ACS Nano* **2011**, *5*, 9494–9500.
12. Talgorn, E.; Abellon, R.; Kooyman, P. J.; Piris, J.; Savenije, T. M.; Goossens, A.; Houtepen, A. J.; Siebbeles, L. D. A. Supercrystals of CdSe Quantum Dots with High Charge Mobility and Efficient Electron Transport to TiO_2. *ACS Nano* **2010**, *4*, 1723–1731.
13. Choi, H; Nicolaescu, R.; Paek, S.; Ko, J.; Kamat, P. V. Supersensitization of CdS Quantum Dots with a Near-Infrared Organic Dye: Towards the Design of Panchromatic Hybrid-Sensitized Solar Cells. *ACS Nano* **2011**, *5*, 9238–9245.
14. Jin, S.; Lian, T. Electron Transfer Dynamics from Single CdSe/ZnS Quantum Dots to TiO_2 Nanoparticles. *Nano Lett.* **2009**, *9*, 2448–2454.
15. Hamada, M.; Nakanishi, S.; Itoh, T.; Ishikawa, M.; Biju, V. Blinking Suppression in CdSe/ZnS Single Quantum Dots by TiO_2 Nanoparticles. *ACS Nano* **2010**, *4*, 4445–4454.
16. Brown, P.; Kamat, P. V. Quantum Dot Solar Cells. Electrophoretic Deposition of CdSe–C_{60} Composite Films and Capture of Photogenerated Electrons with nC_{60} Cluster Shell. *J. Am. Chem. Soc.* **2008**, *130*, 8890–8891.
17. Song, N.; Zhu, H.; Jin, S.; Zhan, W.; Lian, T. Poisson-Distributed Electron-Transfer Dynamics from Single Quantum Dots to C_{60} Molecules. *ACS Nano* **2011**, *5*, 613–621.
18. Gocalińska, A.; Saba, M.; Quochi, F.; Marceddu, M.; Szendrei, K.; Gao, J.; Loi, M. A.; Yarema, M.; Seyrkammer, R.; Heiss, W.; et al. Size-Dependent Electron Transfer from Colloidal PbS Nanocrystals to Fullerene. *J. Phys. Chem. Lett.* **2010**, *1*, 1149–1154.
19. Guldi, D. M.; Zilbermann, I.; Anderson, G.; Kotov, N. A.; Tagmatarchis, N.; Prato, M. Versatile Organic (Fullerene)–Inorganic (CdTe Nanoparticle) Nanoensembles. *J. Am. Chem. Soc.* **2004**, *126*, 14340–14341.
20. Xu, Z.; Cotlet, M. Quantum Dot–Bridge–Fullerene Heterodimers with Controlled Photoinduced Electron Transfer. *Angew. Chem., Int. Ed.* **2011**, *50*, 6079–6083.
21. Hossain, M. A.; Jennings, J. R.; Koh, Z. Y.; Wang, Q. Carrier Generation and Collection in CdS/CdSe-sensitized SnO_2 Solar cells Exhibiting Unprecedented Photocurrent Densities. *ACS Nano* **2011**, *5*, 3172–3181.
22. Jin, S.; Song, N.; Lian, T. Suppressed Blinking Dynamics of Single QDs on ITO. *ACS Nano* **2010**, *4*, 1545–1552.
23. Kuciauskas, D.; Lin, S.; Seely, G. R.; Moore, A. L.; Moore, T. A.; Gust, D.; Drovetskaya, T.; Reed, C. A.; Boyd, P. D. W. Energy and Photoinduced Electron Transfer in Porphyrin-Fullerene Dyads. *J. Phys. Chem.* **1996**, *100*, 15926–15932.
24. Sutton, L. R.; Schloske, M.; Pirner, S.; Hirsch, A.; Guldi, D. M.; Gisselbrecht, J.-P. Unexpected Change in Charge Transfer Behavior in a Cobalt (II) Porphyrin–Fullerene Conjugate That Stabilizes Radical Ion Pair States. *J. Am. Chem. Soc.* **2004**, *126*, 10370–10381.
25. Tkachenko, N. V.; Rantala, L.; Tauber, A. Y.; Helaja, J.; Hynninen, P. V.; Lemmetyinen, H. Photoinduced Electron Transfer in Phytochlorin-[60] Fullerene Dyads. *J. Am. Chem. Soc.* **1999**, *121*, 9378–9387.
26. Imahori, H.; El-Khouly, M. E.; Fujitsuka, M.; Ito, O.; Sakata, Y.; Fukuzumi, S. Solvent Dependence of Charge Separation and Charge Recombination Rates in Porphyrin–Fullerene Dyad. *J. Phys. Chem. A* **2001**, *105*, 325–332.
27. Kanematsu, M.; Naumov, P.; Kojima, T.; Fukuzumi, S. Intermolecular and Intramolecular Photoinduced Electron

Transfer from Planar and Nonplanar Metalloporphyrins to p-Quinones. *Chem.—Eur. J.* **2011**, *17*, 12372–12384.
28. Chen, W.; El-Khouly, M.; Fukuzumi, S. Saddled Distortion of a Sterically Unhindered Porphyrin Ring in a Copper Porphyrin with Electron-Donating Substituents. *Inorg. Chem.* **2011**, *50*, 671–678.
29. De Bettignies, R.; Nicolas, Y.; Blanchard, P.; Levillain, E.; Nunzi, J.-M.; Roncali, J. Planarized Star-Shaped Oligothiophenes as a Newclass of Organic Semiconductors for Heterojunction Solar Cells. *Adv. Mater.* **2003**, *15*, 1939–1943.
30. Uhrich, C.; Schueppel, R.; Petrich, A.; Pfeiffer, M.; Leo, K.; Brier, E.; Kilickiran, P.; Bäuerle, P. Organic Thin-Film Photovoltaic Cells Based on Oligothiophenes with Reduced Band gap. *Adv. Funct. Mater.* **2007**, *17*, 2991–2999.
31. Kreher, D.; Hudhomme, P.; Gorgues, A.; Luo, H.; Araki, Y.; Ito, O. Photoinduced Electron Transfer Processes of a Fused C_{60}−TTF−C_{60} Dumbbell Triad. *Phys. Chem. Chem. Phys.* **2003**, *5*, 4583–4587.
32. Díaz, M. C.; Lllescas, B. M.; Martín, N.; Viruela, R.; Viruela, P. M.; Ortí, E.; Brede, O.; Zilbrermann, I.; Guldi, D. M. Highly Conjugated p-Quinonoid pi-Extended Tetrathiafulvalene Derivatives: A Class of Highly Distorted Electron Donors. *Chem.—Eur. J.* **2004**, *10*, 2067–2077.
33. Imahori, H.; Cardoso, S.; Tatman, D.; Lin, S.; Noss, L.; Seely, G. R.; Sereno, L.; Silber, C.; Moore, T. A.; Moore, A. L.; et al. Photoinduced Electron Transfer in a Carotenobuckminsterfullerene Dyad. *Photochem. Photobiol.* **1995**, *62*, 1009–1014.
34. Williams, R. M.; Zwier, J. M.; Verhoeven, J. M. Photoinduced Intramolecular Electron Transfer in a Bridged C_{60} (Acceptor)-Aniline (Donor) System. Photophysical Properties of the First "Active" Fullerene Diad. *J. Am. Chem. Soc.* **1995**, *117*, 4093–4099.
35. Komamine, S.; Fujitsuka, M.; Ito, O.; Moriwaki, K.; Miyata, T.; Ohno, T. Synthesis, Charge-Separated State Characterization of N-methyl-2-(4′- N-ethylcarbozole)-3-Fulleropyrrolidine and its Derivatives. *J. Phys. Chem. A* **2000**, *104*, 11497–11504.
36. Biju, V.; Barazzouk, S.; Thomas, K. G.; George, M. V.; Kamat, P. V. Photoinduced Electron Transfer between 1,2,5-Triphenylpyrrolidinofullerene Cluster Aggregates and Electron Donors. *Langmuir* **2001**, *17*, 2930–2936.
37. Medintz1, I. L.; Uyeda, H. T.; Goldman, E. R.; Mattoussi, H. Quantum Dot Bioconjugates for Imaging, Labelling and Sensing. *Nat. Mater.* **2005**, *4*, 435–446.
38. Yin, Y.; Alivisatos, A. P. Colloidal Nanocrystal Synthesis and the Organic−Inorganic Interface. *Nature* **2005**, *437*, 664–670.
39. Somers, R. C.; Bawendi, M. G.; Nocera, D. G. CdSe Nanocrystal Based Chem-/Bio- Sensors. *Chem. Soc. Rev.* **2007**, *36*, 579–591.
40. Nirmal, M.; Brus, L. Luminescence Photophysics in Semiconductor Nanocrystals. *Acc. Chem. Res.* **1999**, *32*, 407–414.
41. Biju, V.; Itoh, T.; Ishikawa, M. Delivering Quantum Dots to Cells: Bioconjugated Quantum Dots for Targeted and Nonspecific Extracellular and Intracellular Imaging. *Chem. Soc. Rev.* **2010**, *39*, 3031–3056.
42. Biju, V.; Itoh, T.; Anas, A.; Sujith, A.; Ishikawa, M. Semiconductor Quantum Dots and Metal Nanoparticles: Syntheses, Optical Properties, and Biological Applications. *Anal. Bioanal. Chem.* **2008**, *391*, 2469–2495.
43. Schaller, R. D.; Klimov, V. I. High Efficiency Carrier Multiplication in PbSe Nanocrystals: Implications for Solar Energy Conversion. *Phys. Rev. Lett.* **2004**, *92*, 186601–186604.
44. Guldi, D. M.; Prato, M. Excited-State Properties of C_{60} Fullerene Derivatives. *Acc. Chem. Res.* **2000**, *33*, 695–703.
45. Rühle, S.; Shalom, M.; Zaban, A. Quantum-Dot-Sensitized Solar Cells. *Chem. Phys. Chem.* **2010**, *11*, 2290–2304.
46. Sun, Y.-P.; Ma, B.; Bunker, C. E.; Liu, B. All-Carbon Polymers (Polyfullerenes) from Photochemical Reactions of Fullerene Clusters in Room-Temperature Solvent Mixtures. *J. Am. Chem. Soc.* **1995**, *117*, 12705–12711.
47. Park, J. J.; Lacerda, S. L. D. P.; Stanley, S. K.; Vogel, B. M.; Kim, S.; Douglas, J. F.; Raghvan, D.; Karim, A. Langmuir Adsorption Study of the Interaction of CdSe/ZnS Quantum Dots with Model Substrates: Influence of Substrate Surface Chemistry and pH. *Langmuir* **2009**, *25*, 443–450.
48. Efros, A. L.; Rosen, M. Random Telegraph Signal in the Photoluminescence Intensity of a Single Quantum Dot. *Phys. Rev. Lett.* **1997**, *78*, 1110–1113.
49. Biju, V.; Micic, M.; Hu, D.; Lu, H. P. Intermittent Single-Molecule Interfacial Electron Transfer Dynamics. *J. Am. Chem. Soc.* **2004**, *126*, 9374–9381.
50. Guldi, D. M.; Maggini, M.; Scorrano, G.; Prato, M. Intramolecular Electron Transfer in Fullerene/Ferrocene Based Donor−Bridge−Acceptor Dyads. *J. Am. Chem. Soc.* **1997**, *119*, 974–980.
51. Uyeda, H. T.; Medintz, I. L.; Jaiswal, J. K.; Simon, S. M.; Mattoussi, H. Synthesis of Compact Multidentate Ligands to Prepare Stable Hydrophilic Quantum Dot Fluorophores. *J. Am. Chem. Soc.* **2005**, *127*, 3870–3878.